

# *Dynamic contact angle at nano-scale: a unified view*

Article

Accepted Version

Lukyanov, A. V. and Likhtman, A. E. (2016) Dynamic contact angle at nano-scale: a unified view. ACS Nano, 10 (6). pp. 6045-6053. ISSN 1936-086X doi: <https://doi.org/10.1021/acsnano.6b01630> Available at <https://centaur.reading.ac.uk/65815/>

It is advisable to refer to the publisher's version if you intend to cite from the work. See [Guidance on citing](#).

Published version at: <http://pubs.acs.org/doi/abs/10.1021/acsnano.6b01630>

To link to this article DOI: <http://dx.doi.org/10.1021/acsnano.6b01630>

Publisher: American Chemical Society

All outputs in CentAUR are protected by Intellectual Property Rights law, including copyright law. Copyright and IPR is retained by the creators or other copyright holders. Terms and conditions for use of this material are defined in the [End User Agreement](#).

[www.reading.ac.uk/centaur](http://www.reading.ac.uk/centaur)

**CentAUR**

Central Archive at the University of Reading

Reading's research outputs online

# Dynamic Contact Angle at Nano-Scale: a Unified View.

Alex V. Lukyanov<sup>\*</sup> and Alexei E. Likhtman<sup>†</sup>

*School of Mathematical and Physical Sciences, University of Reading, Reading RG6 6AX,  
UK*

E-mail: a.lukyanov@reading.ac.uk

## Abstract

Generation of dynamic contact angle in the course of wetting is a fundamental phenomenon of nature. Dynamic wetting processes have a direct impact on flows at nano-scale, and therefore their understanding is exceptionally important to emerging technologies. Here, we reveal the microscopic mechanism of dynamic contact angle generation. It has been demonstrated using large-scale molecular dynamics simulations of bead-spring model fluids that the main cause of local contact angle variations is the distribution of microscopic force acting at the contact line region. We were able to retrieve this elusive force with high accuracy. It has been directly established that the force distribution can be solely predicted on the basis of a general friction law for liquid flow at solid surfaces by Thompson & Troian. The relationship with the friction law provides both an explanation of the phenomenon of dynamic contact angle and a methodology for future predictions. The mechanism is intrinsically microscopic, universal and irreducible, and is applicable to a wide range of problems associated with wetting phenomena.

Keywords: *wetting, nano-scale, dynamic contact angle, non-linear friction, molecular dynamics simulations.*

Modelling capillary flows is a general problem in science and industry.<sup>1-4</sup> It requires the knowledge of the dynamic contact angle, which is the boundary condition for flows with moving contact lines.<sup>5,6</sup> At the moment, simulation of capillary flows and interpretation of dynamic contact angle measurements are based on several, quite different phenomenological models and various numerical techniques involving different assumptions about the physical mechanisms and the length scales of the effect.<sup>1,4-28</sup> Macroscopic models appeal to hydrodynamic mechanisms to explain the observed dynamic contact angles, such as free surface viscous bending, hydrodynamic stresses developed in the proximity of the contact line or non-equilibrium surface tensions.<sup>1,5,6,8,16,22,27</sup> In particular, Cox-Voinov model,<sup>5,8</sup> which is basically an asymptotic solution to the Navier-Stokes equations, attributes observed, apparent dynamic contact angles to the free surface bending accompanied by variations of the true, microscopic contact angle with the velocity of the contact line. The formulation is equivalent to modelling the Navier-Stokes equations with a slip condition on the solid boundary and with the true contact angle set as the boundary condition to determine the free surface shape. Experiments have confirmed that the asymptotic solution can accurately reproduce the interface shape in dynamic conditions provided that the microscopic contact angle or/and another material parameter of the model are velocity dependent.<sup>12</sup> From another perspective, in the interface formation theory,<sup>16</sup> the actual dynamic contact angle is part of the entire hydrodynamic solution through the Young-Dupré equation and the variable surface tensions acting on the contact line. The formulation utilizes a modified, different from Cox-Voinov model, set of boundary conditions, which include surface tension gradients as macroscopic hydrodynamic variables. Microscopic molecular-kinetic theory (MKT), on the other hand, postulates concentrated an out-of-balance force of non-hydrodynamic origin, which acts on the three-phase contact line and generates out-of-equilibrium molecular displacements, which are interpreted in terms of the contact line velocity.<sup>7,15,19-21</sup>

At the moment, it is difficult to pick up any particular model of dynamic wetting for applications using only macroscopic observations of dynamic contact angles. All models found

reasonable agreement with macroscopic experiments.<sup>15–17,21</sup> Moreover, even high-resolution measurements at nano-scale<sup>28</sup> have proven difficult to single out any particular theoretical model and to establish the fundamental mechanism of the effect. The best overall performance in matching experimental data has been demonstrated by a combined model, where the microscopic contact angle was set according to the MKT and the interfacial shape was calculated from Cox-Voinov model.<sup>14,15</sup> This was an indication that the microscopic events in the immediate vicinity of the contact line and macroscopic effects due to hydrodynamic stresses do co-exist, can be separated and regarded as complementary. The microscopic contact angle variations with the velocity have been clearly observed in molecular dynamics simulations (MDS) and in the experiments at nano-scale.<sup>15,19–21,26,28</sup> In the same study,<sup>28</sup> it has been implied that there is an additional, unusual convex interface bending, as opposed to the concave bending predicted by Cox-Voinov model, in the region of tens of nanometres at the contact line. Whether or not this additional bending exists and can be accommodated within the framework of the standard hydrodynamic theory is to be seen and verified independently. Apparently, irrespective of that, the main factor of uncertainty now is the generation mechanism of the microscopic dynamic contact angle, which has not been established. What is really happening at the contact line and in what length scale? Is this all due to non-equilibrium surface tensions or the concentrated friction force postulated in the MKT or both or may be something else? Clearly, once the contact line region is fully understood, one can properly address the macroscopic events.

The lack of understanding the fundamental processes involved in the formation of dynamic contact angle makes any new predictions practically very difficult and calls for the use of microscopic modelling. Here we examine the three-phase contact line region in non-equilibrium with MDS where the contact line zone can be clearly resolved and separated from the bulk flow. In our simulations a large cylindrical liquid droplet consisting of 60000 – 90000 particles of mass  $m_f$  is forced to move with constant velocity between two identical solid substrates, Fig. 1. Each substrate (see Methods for details) consists of three  $[0, 0, 1]$  face-

centered cubic (fcc) lattice layers of particles of mass  $m_w = 10m_f$ . Both substrate and liquid particles interact *via* the Lennard-Jones (LJ) potentials  $\Phi_{LJ}^{ij}(r) = 4\epsilon_{ij} \left( \left( \frac{\sigma_{ij}}{r} \right)^{12} - \left( \frac{\sigma_{ij}}{r} \right)^6 \right)$  with the cut-off distance  $2.5\sigma_{ij}$ . Here  $r$  is the distance between the particles,  $\epsilon_{ij}$  and  $\sigma_{ij}$  are characteristic energy and length scales.

The geometry of our nano-scale simulations (see Methods for details) is periodic in the  $x$ -direction with reflective boundary conditions at the simulation box ends in the  $z$ -direction, Fig. 1. The layer thickness in the periodic  $x$ -direction (droplet depth) was set at  $\Delta x \simeq 18\sigma_{ff}$  for the simulations with short chain molecules  $N_b \leq 5$  and at  $\Delta x \simeq 28\sigma_{ff}$  for those ones involving longer chains. The solid wall particles were moving with velocity  $U$  in the  $z$ -direction ( $[1,0,0]$  crystallographic direction) where the reflective wall acted as a piston to mimic forced wetting regime. After initial equilibration during  $\Delta t_{eq} = 10000\tau_0$  with the time integration step  $\Delta t_s = 0.01\tau_0$  ( $\tau_0 = \sigma_{ff}\sqrt{\frac{m_f}{\epsilon_{ff}}}$ ), which was used in the study, we reached a steady state and measured dynamic contact angle and interfacial parameters.

The contact angle in our study has been inferred from the free-surface profiles defined as the locus of equimolar points and averaged during  $5000\tau_0$ . The profiles were developed by means of a three-parameter  $(R, y_0, z_0)$  circular fit  $(y - y_0)^2 + (z - z_0)^2 = R^2$ . The circular fit has been applied to a part of the free-surface profile of length  $\approx 20\sigma_{ff}$  excluding  $4\sigma_{ff}$  layer adjacent to the substrate corresponding to the liquid-solid interface, Fig. 2. One may notice that the interface shape is very well described by the fit, Fig. 1.

## Results and Discussion

The dynamic contact angle collective set of data in the range of Reynolds numbers  $0.005 < Re < 6$  ( $Re = \frac{\rho_b U H}{2\mu}$  was based on half the distance between the substrates  $H/2$ , the bulk particle density  $\rho_b$  and the zero shear rate viscosity  $\mu$ , Table 1) for fluids with different chain length  $N_B$  obtained at different temperatures  $T$ , liquid-solid interactions  $\epsilon_{wf}$  and substrate densities  $\Pi_S$  is shown in Fig. 1 with the parameters summarized in Table 1. The data are represented in terms of the out-of-balance surface tension force  $F = \gamma_{GS} - \gamma_{LS} - \gamma_{LV} \cos \theta$

using the static values of surface tensions  $\gamma_{LV}$ ,  $\gamma_{LS}$  and  $\gamma_{GS}$ , Table 1, and normalized using parameters  $(F^*, U^*)$  of a two-parameter fit  $F_c = F^* \frac{U/U^*}{(1+(U/U^*)^2)^{0.45}}$ , Fig. 1. Here,  $\theta$  is non-equilibrium dynamic contact angle,  $\gamma_{LV}$ ,  $\gamma_{LS}$  and  $\gamma_{GS}$  are equilibrium liquid-gas, liquid-solid of the liquid and gas-solid of the gas (in the approximation of undeformable solid substrate) surface tensions respectively (see Methods for details). We note that the characteristic values of the dynamic contact angle found in our simulations are in accord with the previous observations of dynamic contact angle in droplet relaxation MDS experiments in.<sup>20</sup>

As is seen in Fig. 1, after normalization the data nicely collapse on a single master curve indicating that there is a universal mechanism operating in all those cases. The velocity dependence of the out-of-balance force demonstrates the standard trend routinely observed in experiments on dynamic contact angle - monotonic increase with velocity increases.<sup>12,15,17</sup> Given that surface tension relaxation time in simple interfaces of our LJ liquids is practically zero,<sup>29</sup> all surface tensions of the liquid are expected to be at equilibrium values. This implies that the out-of-balance surface tension force  $F$  can only be balanced by a friction force from the substrate. Using the steady state conditions achieved in our simulations and averaging over five independent runs, it was possible to accurately measure distribution of the friction force acting on the first liquid mono-layer adjacent to the substrate, as is shown in Fig. 2. Typical profile of the friction force tangential to the substrate component  $\delta F$  and corresponding distributions of surface density and tangential surface velocity (quantities averaged over the observation layer  $\Delta y = 1.1 \sigma_{ff}$ ) are shown in Fig. 2.

One can observe that the friction force distribution has a characteristic maximum at  $z \approx 3 \sigma_{ff}$ , counting from the surface density equimolar point. Further away from the equimolar point, after  $z_c \approx 12 \sigma_{ff}$ , the friction force drops to a constant value  $f_\infty$  in the bulk where, at the same time, both surface density and surface velocity distributions attain constant values  $\rho_\infty$  and  $v_\infty$ . One can assume that this point  $z_c$  defines the boundary and the characteristic size of the contact line region in non-equilibrium. Indeed, to account for the observed dynamic contact angle  $\theta$  according to the modified Young-Dupré equation  $\gamma_{LV} \cos \theta = -\gamma_{LS} +$

Table 1: Parameters of the simulations in the moving droplet problem at  $H = 60 \sigma_{ff}$ , Fig. 1. Fluid temperature  $T$ , number of monomers per chain  $N_B$ , the bulk fluid monomer density  $\rho_b$ , bulk shear viscosity  $\mu$ , wall-fluid interaction energy  $\epsilon_{wf}$ , wall density  $\Pi_s$ , liquid-vapour, liquid-solid and solid-vapour surface tensions  $\gamma_{LV}$ ,  $\gamma_{LS}$  and  $\gamma_{GS}$  (in the approximation of undeformable solid substrate), static contact angle  $\theta_0$  (calculated *via* the Young-Dupré equation and measured geometrically), and parameters  $F^*$  and  $U^*$  of the fit  $F_c = F^* \frac{U/U^*}{(1+(U/U^*)^2)^{0.45}}$ . Here, velocity  $U^*$  was normalized by  $u_0 = \sqrt{\epsilon_{ff}/m_f}$ , densities  $\rho_b$  and  $\Pi_s$  by  $\rho_0 = \sigma_{ff}^{-3}$ , viscosity  $\mu$  by  $\mu_0 = \sqrt{\epsilon_{ff} m_f}/\sigma_{ff}^2$ , surface tensions and  $F^*$ , which is the force per unit length, by  $\gamma_0 = \epsilon_{ff}/\sigma_{ff}^2$ . <sup>†</sup> The shear viscosity was obtained as in ref<sup>37</sup> under bulk conditions in the limit of zero shear rates. <sup>††</sup>The static contact angle  $\theta_0$  here is inferred from the Young-Dupré equation  $\gamma_{LV} \cos \theta_0 = -\gamma_{LS} + \gamma_{GS}$ . <sup>‡</sup>The static contact angle  $\theta_0$  here is obtained from the free-surface profiles of cylindrical drops.

Run	$T \frac{k_B}{\epsilon_{ff}}$	$N_B$	$\rho_b$	$\mu^\dagger$	$\epsilon_{wf}/\epsilon_{ff}$	$\Pi_s$	$\gamma_{LV}$	$\gamma_{LS}$	$\gamma_{GS}$	$\theta_0^{\dagger\dagger}$	$\theta_0^\dagger$	$F^*$	$U^*$
(a)	0.8	5	0.91	10.5	0.9	4	$0.92 \pm 0.04$	$-0.66 \pm 0.03$	0	$44 \pm 4^\circ$	$39 \pm 3^\circ$	$1.14 \pm 0.02$	$0.02 \pm 0.001$
(b)	0.8	5	0.91	10.5	0.65	4	$0.92 \pm 0.04$	$-0.02 \pm 0.05$	0	$89 \pm 3^\circ$	$92 \pm 4^\circ$	$0.67 \pm 0.02$	$0.034 \pm 0.003$
(c)	0.8	5	0.91	10.5	0.5	1.4	$0.92 \pm 0.04$	$0.25 \pm 0.04$	0	$106 \pm 4^\circ$	$108 \pm 5^\circ$	$0.59 \pm 0.04$	$0.07 \pm 0.02$
(d)	0.8	5	0.91	10.5	1.2	1.4	$0.92 \pm 0.04$	$-2.3 \pm 0.07$	0	$0^\circ$	$0^\circ$	$2.29 \pm 0.02$	$0.009 \pm 0.001$
(e)	0.8	1	0.73	1.2	0.65	4	$0.36 \pm 0.02$	$-0.22 \pm 0.02$	$-0.08 \pm 0.01$	$67 \pm 4^\circ$	$64 \pm 3^\circ$	$0.43 \pm 0.01$	$0.11 \pm 0.01$
(f)	0.8	15	0.93	30	0.9	4	$1.05 \pm 0.04$	$-0.63 \pm 0.05$	0	$53 \pm 4^\circ$	$49 \pm 5^\circ$	$1.08 \pm 0.05$	$0.007 \pm 0.001$
(g)	1	15	0.88	18	0.8	4	$0.83 \pm 0.04$	$-0.21 \pm 0.04$	0	$75 \pm 3^\circ$	$75 \pm 3^\circ$	$0.74 \pm 0.02$	$0.027 \pm 0.002$
(h)	1	30	0.89	34	0.8	4	$0.89 \pm 0.04$	$-0.19 \pm 0.04$	0	$78 \pm 3^\circ$	$79 \pm 4^\circ$	$0.73 \pm 0.02$	$0.014 \pm 0.002$

$\gamma_{GS} - F$ , it is sufficient to integrate the friction force distribution  $\delta F(z)$  within this zone to obtain the necessary total force  $F$ . For example, in case (a) from Table 1 at  $U = 0.1 u_0$ ,  $u_0 = \sqrt{\epsilon_{ff}/m_f}$ , the dynamic contact angle is  $\theta = 136^\circ$ , Table 2, the total force per unit length  $F = 1.32 \gamma_0$  and the distribution should be integrated  $F = \int_{-\infty}^{z_c} \delta F dz$  to  $z_c = 7.5 \sigma_{ff}$ . In general, the size of the contact line region defined through the integration interval  $-\infty < z \leq z_c$  varied between the cases in the range  $6.5 \sigma_{ff} \leq z_c \leq 14.3 \sigma_{ff}$ , see Table 2.

Consider now distributions of surface density and surface velocity, as they play a crucial role in the behaviour of the friction force and the effect of the dynamic contact angle. The surface density distribution is found to have one characteristic length scale  $\Delta_\rho$  and can be accurately approximated by a hyperbolic tangent two parameter fit, see Fig. 2(d),  $\rho_s(z) = \rho_\infty \bar{\rho}_s(z) = \rho_\infty \psi_0(z, \Delta_\rho, z_0)$ ,  $\psi_0(z) = \frac{1}{2} \left( 1 + \tanh \left( \frac{z-z_0}{\Delta_\rho} \right) \right)$ , where  $z_0$  is the equimolar point, which is taken as the reference point in this study, that is  $z_0 = 0$ . The length scale  $\Delta_\rho$  is relatively short in comparison with the contact line zone defined by  $z_c$ , Table 2, and is basically the apparent (widened by capillary waves<sup>30</sup>) width of the liquid-gas interface.

Table 2: Parameters of the simulations in the moving droplet. The droplet width  $H$ , substrate velocity  $U$ , dynamic contact angle  $\theta$ , parameters of the friction force-velocity distribution (1),  $f^*$  and  $v^*$ , the length scale of surface density distribution  $\Delta_\rho$ , parameters of surface velocity  $v_s$  distribution  $z_1, z_2$  and  $\Delta_{v2}$  obtained at  $\Delta_{v1} = \Delta_\rho$ , the integration lengths to calculate the total force  $F$  from the force distribution  $z_c$  in the MDS simulations and  $z_c^\infty$  in macroscopic limit, slip lengths  $L_0^s$  and  $L_U^s$  in the linear regime ( $v_s < v^*$ ) and at  $v_s = U$  obtained from the friction law through  $L^s(v_s) = \frac{\mu v_s}{f_s}$ , and the ratio of self-diffusion approximation coefficients  $B^* = \rho_\infty B_1/B_0$ . Here, all the length scales were normalized by  $\sigma_{ff}$ , velocities by  $u_0$ ,  $u_0 = \sqrt{\epsilon_{ff}/m_f}$ , and parameter  $f^*$ , which is the force per unit area, by  $f_0 = \epsilon_{ff}/\sigma_{ff}^3$ .

Run	$H$	$U$	$\theta$	$f^*$	$v^* \cdot 10^2$	$\Delta_\rho$	$z_1$	$z_2$	$\Delta_{v2}$	$z_c$	$z_c^\infty$	$L_0^s$	$L_U^s$	$B^*$
(a)	45	0.1	$135 \pm 5^\circ$	$0.31 \pm 0.01$	$1.2 \pm 0.1$	$1.4 \pm 0.01$	$-0.8 \pm 0.1$	$-1 \pm 0.1$	$3.9 \pm 0.1$	6.8	8.5	0.4	1.4	$-0.94 \pm 0.01$
(a)	60	0.1	$136 \pm 5^\circ$	$0.31 \pm 0.01$	$1.2 \pm 0.1$	$1.5 \pm 0.01$	$-0.9 \pm 0.1$	$-1 \pm 0.1$	$4.1 \pm 0.1$	7.5	8.5	0.4	1.4	$-0.94 \pm 0.01$
(a)	100	0.1	$145 \pm 5^\circ$	$0.31 \pm 0.01$	$1.2 \pm 0.1$	$1.9 \pm 0.01$	$-1.3 \pm 0.1$	$-0.7 \pm 0.1$	$3.8 \pm 0.1$	9.2	9.8	0.4	1.4	$-0.94 \pm 0.01$
(a)	60	0.05	$124 \pm 5^\circ$	$0.31 \pm 0.01$	$1.2 \pm 0.1$	$1.3 \pm 0.01$	$-0.1 \pm 0.04$	$-0.5 \pm 0.1$	$4.2 \pm 0.1$	11.6	9.5	0.4	0.95	$-0.94 \pm 0.01$
(a)	60	0.03	$113 \pm 4^\circ$	$0.31 \pm 0.01$	$1.2 \pm 0.1$	$1.2 \pm 0.01$	$-0.01 \pm 0.03$	$-1.1 \pm 0.1$	$5.5 \pm 0.2$	13.2	10.5	0.4	0.73	$-0.94 \pm 0.01$
(b)	60	0.1	$138 \pm 5^\circ$	$0.3 \pm 0.01$	$4.6 \pm 0.3$	$1.6 \pm 0.01$	$-1.1 \pm 0.04$	$-1.8 \pm 0.2$	$5.0 \pm 0.2$	6.5	8	1.6	2.6	$-0.89 \pm 0.01$
(d)	60	0.06	$123 \pm 5^\circ$	$0.28 \pm 0.02$	$0.3 \pm 0.05$	$1.3 \pm 0.01$	$0.6 \pm 0.05$	$-0.3 \pm 0.2$	$4.3 \pm 0.2$	14.3	9	0.1	0.66	$-0.95 \pm 0.03$
(g)	60	0.09	$141 \pm 5^\circ$	$0.37 \pm 0.01$	$5 \pm 0.4$	$1.8 \pm 0.02$	$-1.4 \pm 0.1$	$-1.3 \pm 0.1$	$4.3 \pm 0.1$	7.6	8.5	2.7	7.3	$-0.89 \pm 0.01$

Some variations of  $\Delta_\rho$  observed between the cases were likely due to different contact angles. Corrected quantity  $\Delta'_\rho = \Delta_\rho \cos(\theta - \pi/2)$ , taking into account the effect of inclination angle, showed no such variations  $1 \sigma_{ff} \leq \Delta'_\rho \leq 1.1 \sigma_{ff}$ , and was close to our direct measurements of liquid-gas interface width  $\Delta'_\rho = 0.82 \sigma_{ff}$  at  $T = 0.8$  and  $\Delta'_\rho = 1.1 \sigma_{ff}$  at  $T = 1$ .

The surface velocity distribution has two characteristic length scales  $\Delta_{v1}$  and  $\Delta_{v2}$ , and can be approximated by a five parameter fitting function, Fig 2(e),  $v_s(z) = v_\infty f_v(z)$ ,  $f_v(z) = \psi_0(z, \Delta_{v1}, z_1) \psi_0(z, \Delta_{v2}, z_2)$ . The first length scale  $\Delta_{v1}$  was found to be very close to  $\Delta_\rho$  and was apparently driven by the density variations. Therefore, it was possible to set  $\Delta_{v1} = \Delta_\rho$  and reduce the number of fitting parameters. The second length scale  $\Delta_{v2}$  was of the order of the contact line zone defined by  $z_c$ . Remarkably, it showed no dramatic variations between the cases, Table 2. We note, that variations of the tangential surface velocity component were accompanied by variations of the normal surface velocity component  $v_n$  (normal vector pointing into the surface layer), Fig. 2(d). That is there was strong mass exchange in the contact line region, with the mass conservation  $\rho_s v_n = \rho_s \Delta y \frac{\partial v_s}{\partial z}$ ,  $\Delta y = 1.1 \sigma_{ff}$ , being perfectly observed in our MDS, insert in Fig. 2(e).

Away from the contact line region, the flow is rectilinear Hagen-Poiseuille flow where both



velocity  $v_\infty$  and the friction force  $f_\infty$  are defined by the shear rate in the bulk. Changing the distance between the substrates  $H$ , one can vary the shear rate and the force value  $f_\infty$ , Fig. 2(a). We note that the maximum value of the friction force  $f_M$  is also affected by the value of the bulk shear rate but to a much lesser extent. Using the inverse distance  $H^{-1}$  as a parameter, one can extrapolate the values of  $f_\infty$  and  $f_M$  in the macroscopic limit  $H \rightarrow \infty$ . Functions  $f_M(H^{-1})$  and  $f_\infty(H^{-1})$  were found to be linear,  $f_M = 0.14 f_0 + 4.1 H^{-1} f_0 \sigma_{ff}$  and  $f_\infty = 5 \times 10^{-4} f_0 + 7.3 H^{-1} f_0 \sigma_{ff}$ ,  $f_0 = \epsilon_{ff} / \sigma_{ff}^3$ . So that in the macroscopic limit ( $H \rightarrow \infty$  at a fixed substrate velocity  $U$ ) the bulk value goes to zero  $\lim_{H \rightarrow \infty} f_\infty \approx 0$ , as expected, while the force maximum remains finite  $\lim_{H \rightarrow \infty} f_M = 0.14 f_0$ . This is a clear indication that in the macroscopic limit the friction force will be finite and strictly localized in the small region at the contact line. At the same time, it is also obvious that in nano-flows, in contrast to macroscopic systems, there is no very clear separation between the bulk region and the contact line zone. Therefore in nano-systems the dynamic contact angle may be influenced by entire flow conditions. To understand the behaviour of the friction force quantitatively, we will apply friction laws revealed in MDS studies of the slip phenomena using uniform rectilinear flows.<sup>31-35</sup>

For LJ liquids the non-linear friction force-velocity dependence can be described in a range of velocities by a two-parameter relationship

$$f_s = f^* \frac{v_s / v^*}{(1 + (v_s / v^*)^2)^\lambda} \quad (1)$$

with parameter  $\lambda$  found to be  $\lambda \approx 0.35$ .<sup>31-35</sup> Here  $f_s$  is the solid to liquid tangential to the substrate friction force per unit area,  $v_s$  is the slip velocity with respect to a stationary substrate,  $f^*$  is a coefficient of sliding friction and  $v^*$  is a characteristic velocity. Measurements of the friction force on our substrates in the velocity range relevant to our dynamic angle simulations have revealed similar dependence with  $\lambda \approx 0.3$ , Fig. 4, with parameters listed in Table 2. Outside that range, at higher velocities (larger external force) the friction

force quickly reaches its maximum, and the system gets into a runaway regime. MD simulations were performed in a steady flow passing in between two substrates (lateral dimensions  $20 \times 20 \sigma_{ff}$ ) in plane geometry with liquid layer thickness  $\approx 16 \sigma_{ff}$  with periodic boundary conditions. The pressure in the liquid without the applied external force was set to a small level  $p = 0.01 \epsilon_{ff} / \sigma_{ff}^3$  to mimic atmospheric pressure, as it would be in most experiments with open chambers.

To apply this friction law to our problem, one needs to identify the factors influenced by the distribution of density. In previous studies, the coefficient of sliding friction  $f^*$  was found to depend on several parameters, such as contact density in the first fluid mono-layer  $\rho_c$ , in-line structure factor  $S_{q_{\parallel}}$  probed by the first reciprocal lattice vector  $q_{\parallel} = 2\pi\sigma_{ff}/\sigma_{ww}$  of the wall in the direction of shear and the collective self-diffusion coefficient  $D_{q_{\parallel}}$  deduced from  $S_{q_{\parallel}}$ , that is  $f^* \propto \frac{\rho_c S_{q_{\parallel}}}{D_{q_{\parallel}}}$ .<sup>32-35</sup> Note, the collective diffusion coefficient for long-chain molecules reflects internal rearrangements of the chains and not the centre of mass of the molecule.<sup>32</sup>

It is not straightforward to transfer the results obtained in homogeneous flows to our situation given the size of the contact line zone of a few particle diameters where the density and velocity exhibited rapid changes. So, in the current model we will only include major trends. It was assumed that the friction force should be directly proportional to the surface density  $\rho_s(z)$ , as the linear dependence of  $f^*$  on  $\rho_c$  suggests, and inversely proportional to a linearised self-diffusion coefficient  $D_{q_{\parallel}} \propto B_0 + B_1\rho_s$ . The later approximation takes into account a substantial increase in the particle mobility in the low density contact line region. At the same time, due to the presence of surface potentials no divergence is expected as  $\rho_s \rightarrow 0$ , as it would be usually the case in the bulk conditions, where the self-diffusion coefficient  $D$  diverges with the bulk density  $\rho \rightarrow 0$  as  $D \propto \rho^{-1}$ .<sup>36</sup>

Taking this friction law, equation (1), as a model, one can form an analytical expression to calculate the friction force distribution in the coordinate system moving with the contact

line

$$\delta F_m(z) = f^* \frac{\bar{\rho}_s(z)}{\bar{D}(z)} \frac{\frac{U - v_s(z)}{v^*}}{\left(1 + \left(\frac{U - v_s(z)}{v^*}\right)^2\right)^{0.3}}. \quad (2)$$

Here,  $\delta F_m$  is the solid to liquid tangential to the substrate friction force per unit area,  $U - v_s(z)$  is the slip velocity with respect to the moving substrate, and  $f^*$  and  $v^*$  are parameters of the friction law (1) away from the contact line region. Distributions of density and the self-diffusion coefficient were introduced to account for the variations of the coefficient of sliding friction  $f^*$  in the contact line region. The distributions were normalized in such a way,  $\bar{\rho}_s(z) = \rho_s(z)/\rho_\infty$  and  $\bar{D}(z) = \frac{1+B^*\bar{\rho}_s}{1+B^*}$ ,  $B^* = \rho_\infty B_1/B_0$ , that in the bulk  $\bar{\rho}_s = 1$  and  $\bar{D} = 1$ .

**Comparison Between the Model and MDS.** To compare our model force distribution, equation (2), with simulations, we fix parameters of the friction law  $f^*$  and  $v^*$  and the substrate velocity  $U$ , parameters of the surface density and surface velocity distributions  $z_1, z_2, \Delta_\rho, \Delta_{v2}$  and  $v_\infty$  (though allowing parameter  $z_2$  to vary within the length of the measurement interval  $\Delta z \approx 0.7 \sigma_{ff}$ ) leaving only one unknown fitting parameter  $B^*$ , Table 2. The result is shown in Fig. 3(a)-(c) with the obtained values of  $B^*$  listed in Table 2. Corresponding distributions of density  $\rho_s(z)$  and velocity  $v_s(z)$ , approximated in the model by  $\psi_0(z)$  and  $f_v(z)$ , are shown in Fig. 3(d,e). One can see, that the model distribution  $\delta F_m$  correctly identifies the position of the maximum, the shape of the distribution in general and the value in the bulk  $f_\infty$ . Several representative cases with the parameters listed in Table 2 were processed. It was found that the model accurately reproduces the trends observed with variations of shear rates in the bulk (different  $H$ , Fig. 3(a)), variations of the surface potential  $\epsilon_{wf}$  (Fig. 3(c)) and liquid viscosity  $\mu$ , and with variations of the substrate velocity  $U$ , Fig. 3(a,b).

**Macroscopic Limit of the Model.** One can now turn to a more practical question of the macroscopic limit in the model, when the system size is large  $H \gg 1$  while velocity is

still at the level of normal hydrodynamic velocities. In this limit, the shear rates and the slip velocity are relatively small, that is  $v_\infty \approx U$ . Accordingly, one can now set  $v_\infty = U$  in the distribution of velocity approximated by  $f_v$ ,  $v_s(z) = U f_v(z)$ , to calculate distribution of the friction force  $\delta F_m$  using equation (2). To demonstrate the friction force distribution in the macroscopic limit, we will take all parameters of the case (a) from Table 1 at  $H = 100 \sigma_{ff}$  and  $U = 0.1 u_0$  ( $u_0 = \sqrt{\epsilon_{ff}/m_{ff}}$ ) with parameter  $B^*$  set to the value providing the best fit shown in Fig. 3(a). The result is shown in Fig. 3(a) for comparison, the shaded area. It is seen that the force is now strictly located within the finite region inside the contact line zone defined by  $z_c$ . The point where the force value is at 10% of the maximum value  $f_M$ ,  $z_c^\infty$ , can now be used as the definition of the contact line zone in macroscopic limit. Values of  $z_c^\infty$  are listed in Table 2. Remarkably, they show little variations between the cases. We also note that the maximum value of the friction force given by equation (2),  $\max(\delta F_m) \approx 0.16 f_0$ , is close to the value found by the linear extrapolation  $f_M \approx 0.14 f_0$ .

**Mechanism of Dynamic Contact Angle Generation.** The obtained distribution of the localized friction force by means of the relationship (2) and in MDS is the main result of our paper. It provides insights into the fundamental mechanisms of the dynamic wetting phenomena and a methodology for theoretical predictions of the dynamic contact angle effect. Our analysis demonstrates in detail, from the first microscopic principles, how the localized contact line force is generated. In macroscopic modeling this force distribution should be regarded as a "delta" force acting on the contact line. That is, integral of  $\delta F$ ,  $F = \int \delta F dz$  directly contributes into the Young-Dupré equation  $\gamma_{LV} \cos \theta = -\gamma_{LS} + \gamma_{GS} - F$ .

The revealed mechanism is inherently microscopic. It suggests that the contact line force distribution can be accurately determined solely from the knowledge of non-linear friction law, and the distributions of density and velocity in the contact line region. Non-linear friction law can be obtained from experiments or from MDS of simple bead spring models such as those studied here or even atomistic models using simple geometries with no contact lines involved, for example.<sup>31</sup> Distribution of density and its length scale  $\Delta_\rho$  can be also

inferred from experiments and MDS only involving liquid-gas interfaces. Mobility of the particles only affects the friction force distribution in the relatively small part of the contact line zone of the order of  $\Delta_\rho$  and can be approximated without substantial loss of accuracy. The most intricate part in the methodology is determination of velocity distribution and its characteristic length scale  $\Delta_{v2}$ , which in turn defines the contact line zone. We argue that this parameter is directly related to the length scale of the interaction potentials. This explains its weak variations between the cases analyzed in this study and lack of any correlations with linear ( $v_s \ll v^*$ ) and non-linear ( $v_s \sim v^*$ ) slip lengths  $L_0^s$  and  $L_U^s$ , Table 2. One can, of course, determine  $\Delta_{v2}$  directly from MDS and then use it for macroscopic predictions, but how does this length scale appear exactly and how can we approximate it without engaging MDS? Consider distribution of the total tangential force acting on the first liquid mono-layer adjacent to the substrate, that is the friction force  $\delta F$  and the force from the rest of the liquid  $f_{LL}$ , Fig. 3(f). One can see that apart from a region of the order of  $\Delta_\rho$  around the equimolar point  $z = 0$  corresponding to the liquid-gas interface, the total force acting on the particles in the layer is practically zero,  $\delta F + f_{LL} \approx 0$ . This is always the case at equilibrium, when according to the Young-Dupré equation  $\gamma_{LV} \cos \theta_0 = -\gamma_{LS} + \gamma_{GS}$  the surface tension forces are balanced. At non-equilibrium, this implies that in a steady state, when the contact line is already moving with constant velocity, unbalanced molecular forces created as a result of dynamic contact angle, different from the static angle, will be balanced by the friction force. That is the velocity distribution is tuned according to  $f_s(v_s(z)) + f_{LL}(z) = 0$ . This interplay between the molecular and surface friction forces defines the length scale of the contact line zone and its invariance, if the nature and the length scale of the molecular forces are the same.

Once the friction force distribution  $\delta F_m(z)$  is determined, it can be directly used to predict dynamic contact angle *via* the Young-Dupré equation  $\gamma_{LV} \cos \theta = -\gamma_{LS} + \gamma_{GS} - F$ , where  $F = \int_{-\infty}^{\infty} \delta F_m dz$ . Since  $\delta F_m$  is strictly localized, the integral of  $\delta F_m$  quickly converges and can be conveniently taken from  $-\infty$  to  $\infty$ . That is, assuming that friction law has a

form similar to equation (1) with some power  $\lambda$ ,

$$F = f^* \Delta_{v2} \bar{U} \int_{-\infty}^{\infty} \frac{\bar{\rho}_s(\bar{z})}{\bar{D}(\bar{z})} \frac{\Omega(\bar{z})}{(1 + \bar{U}^2 \Omega^2(\bar{z}))^\lambda} d\bar{z} \quad (3)$$

where  $\Omega(\bar{z}) = (1 - f_v(\bar{z}))$  with the new variable  $\bar{z} = z/\Delta_{v2}$  defined according to the contact line length scale and  $\bar{U} = U/v^*$ .  $\bar{U}$  defines the non-linear behavior of the contact line force  $F$  with the contact line velocity. At low velocities,  $\bar{U} \ll 1$  or small capillary numbers  $Ca \ll 1$  ( $Ca = \mu U/\gamma_{LV}$ ) the dependence becomes linear  $F \propto f^* \Delta_{v2} \bar{U}$ ,  $\cos \theta - \cos \theta_0 \propto Ca$ , the trend which is commonly observed in experiments.<sup>4,17,20</sup> An extrapolated dependence of the dynamic contact angle  $\theta$  on the capillary number in the macroscopic limit  $H \gg 1$  using relationship (3) is illustrated in Fig. 5 at  $\lambda = 0.3$ . The data in the plot have been extrapolated by variations of the substrate velocity  $U$  from two particular cases at a given velocity  $U = 0.1 u_0$ , but different values of  $H$  ( $H = 100 \sigma_{ff}$  and  $H = 60 \sigma_{ff}$ ) presented in Fig. 3(a). The obtained dependencies, while generally consistent, demonstrate that the behaviour of the dynamic contact angle is sensitive to the details of microscopic distributions. The key parameter here turns out to be  $\Delta_{v2}$ . Indeed, if the value of  $\Delta_{v2}$  is set in both cases to  $\Delta_{v2} = 3.8 \sigma_{ff}$ , while keeping the other parameters as they were in Table 2, the dependencies become almost identical.

What are the implications of our findings for the developed theories? Apparently, the microscopic contact angle, which may be calculated using (3), provides the necessary boundary condition for macroscopic modelling, either in the form of numerical simulations or asymptotic solutions, such as Cox-Voinov model. The length scales of the friction force distribution and its characteristic amplitudes suggest that other macroscopic effects at the contact line either do not exist or may only serve as corrections to the main effect. In particular, hydrodynamic stresses were seen to give negligible contribution into the force acting on the contact line in the macroscopic limit. They become only important when the system size tends to nano-scale. One can also rule out contributions from non-equilibrium surface tensions, in

particular considering very short relaxation times of the surface phase.<sup>29</sup> At the same time, the MKT hypothesis about concentrated force of microscopic origin acting on the contact line is fully consistent with our results.<sup>7,15,19–21</sup>

**Comparison with the MKT.** At its core, the MKT is based on the Eyring’s phenomenological theory of rate processes<sup>38</sup> applied on average to some region at the contact line. The out-of-balance surface tension force  $\gamma_{LV}(\cos \theta_0 - \cos \theta)$  is related with the unbalanced rate of molecular jumps in the region. The molecular jumps are described by a frequency  $\kappa_0$  and a displacement  $\Lambda_0$  of the order of the atomic distance. The two parameters define a characteristic velocity  $V_c = 2\Lambda_0\kappa_0$  and a characteristic friction force per unit length of the contact line  $\chi_0 = 2\frac{k_B T}{\Lambda_0^2}$ . The net macroscopic result is a quite distinctive contact line force-velocity dependence,

$$F_{MKT} = \chi_0 \ln(U/V_c + \sqrt{1 + (U/V_c)^2}). \quad (4)$$

While the friction force law (4) looks different from the friction force functional forms (1) providing the best fits in our simulations and in the previous works,<sup>31,32,35</sup> it is possible to conjoin them by variation of parameters  $\chi_0$  and  $V_c$ . Application of fit (4) to the normalized friction force-velocity dependence data obtained in homogeneous conditions of the thin film flows is illustrated in Fig. 4, the dashed line. However, the same fit (4) does not match the contact line force-velocity dependence data, the dashed line in Fig. 1. This might be actually expected, given the expression for the total contact line force (3). Apparently, the same functional form seemed very unlikely to simultaneously provide the best description to the friction force-velocity dependence in homogeneous conditions, (1), and to the convolution of the force with velocity and density distributions in inhomogeneous conditions at the contact line, (3).

Here lies the principle difference between the MKT approach and our methodology. The MKT provides a phenomenological treatment, an approximation to the integrated friction

force (3), using the supposition of homogeneity of the contact line zone, while our analysis suggests that particular distributions of surface density and velocity should matter.

From the fit, shown in Fig. 4, one can compare parametric dependencies of  $\chi_0$  and  $V_c$  with our MDS in homogeneous conditions of the thin film flows. According to the MKT,<sup>20</sup> the two parameters scale as  $\chi_0 = 2 \frac{k_B T}{\Lambda_0^2}$  and  $V_c = 2 \frac{\Lambda_0 k_B T}{C_L \mu} \exp \left( \frac{\Lambda_0^2}{k_B T} (\gamma_{LS} - \gamma_{LV}) \right)$ , where  $\mu$  is the zero shear viscosity,  $C_L = \frac{N_B}{\rho_b}$  is the molecular volume of the liquid and  $\rho_b$  is the bulk particle density, Table 1. It has been also established that for the LJ liquids  $\Lambda_0$  is approximately constant and is equal to  $\Lambda_0 \approx 1.2 \sigma_{ff}$ .<sup>20</sup> At the same time, from the fit shown in Fig. 4,  $\chi_0 = f^* \tilde{\chi} \Delta_c$  ( $\tilde{\chi} = 0.8$ ) and  $V_c = v^* \tilde{V}$  ( $\tilde{V} = 0.9$ ), where  $\Delta_c$  is some effective length scale of the contact line zone. The size of the contact line zone is not specified in the MKT, so for comparison one can use half the integration distance  $z_c^\infty$ , Table 2, that is  $\Delta_c \approx 4.5 \sigma_{ff}$ .

The first parametric dependence of  $\chi_0$  is consistent with our observations of  $f^*$ , Table 2. The value of  $f^*$  linearly increases with temperature  $T$ , otherwise being constant, giving approximately  $\Lambda_0 \approx 1.2 \sigma_{ff}$ . The second parametric dependence of  $V_c$  allows to compare variations of  $v^*$ . For example, consider the cases (a), (b), (d) and (g), Table 1 and Table 2. Using the expression for  $V_c$ , its relationship with  $v^*$  and parameters from Tables 1 and 2, one can obtain  $v_a^* \approx 2 \times 10^{-3} f_0$ ,  $v_b^* \approx 7 \times 10^{-3} f_0$ ,  $v_d^* \approx 10^{-4} f_0$  and  $v_g^* \approx 2 \times 10^{-3} f_0$ , as it follows from the MKT scaling,  $f_0 = \epsilon_{ff} / \sigma_{ff}^3$ . One can see that the calculated values are about one order of magnitude off the values measured in the MDS, Table 2. The cause of the discrepancy is not clear at the moment. This could be due to the limitations of the Eyring's phenomenological approach, especially its approximate character for long-chain molecules. The theory is best applied when spherically symmetric molecules spend sufficiently long time in the potential wells formed by the substrate atoms, so that their motion indeed consists of a series of jumps, rather than of continuous trajectories.<sup>38</sup> This may not be the case here. At the same time, one can not rule out the effects of shear thinning.<sup>32</sup> Apparently, more studies of the friction force laws are required.



# Conclusions

To conclude, it has been shown that the main contribution to the effect of dynamic wetting at nano-scale is due to the local variations of microscopic contact angle. The variations of the microscopic contact angle have been directly observed in experiments at nano-scale.<sup>28</sup> Though no substantial effects of nano-bending reported there were found in our MDS. The interface was of a circular shape and the only unusual 'interfacial' distortions were observed within a few atomic distances from the solid substrate, that is in a range of  $\approx 1$  nm, which is within the interfacial layer itself. One needs to note though that the bending observed in<sup>28</sup> was convex and was detected within the length scales of tens of nanometres. It may be 'hidden', if it does exist, in the circular, convex free surface profiles observed in our MDS given the effective system size of the same order - tens of nanometres. Secondly, it has been directly established that the main mechanism of these contact angle variations is non-linear friction force distribution acting on the first monolayer at the solid substrate on the length scale induced by the interaction potential of constituent molecules. The observed length scale defines the size of the contact line zone. The combined effect of the friction force distribution is the integrated total force  $F$ , (3), which manifests itself in macroscopic descriptions as a singular point force acting directly on the contact line and leading to a modified Young-Dupré equation  $\gamma_{LV} \cos \theta = -\gamma_{LS} + \gamma_{GS} - F$ .

# Methods

**Molecular Dynamics Simulations.** We distinguish between liquid (index  $i, j = f$ ) and solid wall (index  $i, j = w$ ) particles. The liquid particles interacting *via* LJ potentials are connected into linear chains of  $N_B = 5$  to 30 beads by the finitely extensible non-linear elastic (FENE) springs, and the strength of the springs is adjusted so that the chains cannot cross each other,  $\Phi_{FENE}(x) = -\frac{k}{2}R_0^2 \ln \left( 1 - \left( \frac{x}{R_0} \right)^2 \right)$ . Here  $x$  is the distance between the beads,  $R_0 = 1.5 \sigma_{ff}$  is the spring maximum extension and  $k = 30 \epsilon_{ff} \sigma_{ff}^{-2}$  is the spring constant

- parameters of the Kremer-Grest model.<sup>39</sup>

The solid wall particles are attached to anchor points forming fcc lattice layers *via* harmonic potential  $\Phi_a = \xi x^2$ , with the strength  $\xi = 800 \frac{\epsilon_{ff}}{\sigma_{ff}^2}$  chosen such that the root-mean-square displacement of the wall atoms was small enough to satisfy the Lindemann criterion for melting  $\sqrt{\langle \delta r^2 \rangle} < 0.15 \sigma_{ww}$ . The strength of the harmonic potential was sufficient to guarantee rigidity of the solid wall, so that elasto-capillarity effects can be neglected, that is  $(\gamma_{LV}/\xi)^{1/2} \ll 1$  ( $\gamma_{LV}$  is equilibrium liquid-gas surface tension).<sup>40</sup> The anchor points in the layer of the solid wall facing the liquid molecules have been slightly randomized in the vertical  $y$  direction, with the amplitude  $\sqrt{\langle \delta y^2 \rangle} = 0.3 \sigma_{ff}$ . This small roughness allowed us to avoid undesirably large slip lengths observed in MDS<sup>32</sup> and any bias towards ideal substrates in this study. The state of the liquid, its temperature  $0.8 \epsilon_{ff}/k_B \leq T \leq 1 \epsilon_{ff}/k_B$  ( $k_B$  is the Boltzmann constant) was controlled by means of a DPD thermostat with the cut-off distance of  $2.5 \sigma_{ff}$  and friction  $\varsigma_{dpd} = 0.5 \tau_0^{-1}$ ,  $\tau_0 = \sigma_{ff} \sqrt{\frac{m_f}{\epsilon_{ff}}}$ , to have minimal side effects on particle dynamics. The substrate density  $\Pi_S$  was controlled by the minimal distance between the solid wall particles  $\sigma_{ww}$ ,  $\Pi_S = 4.1 \sigma_{ff}^{-3}$  ( $\sigma_{ww} = 0.7 \sigma_{ff}$ ) and  $\Pi_S = 1.41 \sigma_{ff}^{-3}$  ( $\sigma_{ww} = \sigma_{ff}$ ). The liquid-solid interaction length scale was set to the minimal distance between solid particles  $\sigma_{wf} = \sigma_{ww}$ .

**Calculation of the Surface Tensions of the Liquid and Verification of the Young-Dupré Equation in Static Conditions.** Before conducting simulations with a moving contact line, a set of measurements in static conditions were done to obtain equilibrium parameters and compare them with the Young-Dupré equation  $\gamma_{LV} \cos \theta_0 = -\gamma_{LS} + \gamma_{GS}$  by placing a cylindrical drop (40000 particles) on the substrate. Here  $\theta_0$  is the static contact angle and  $\gamma_{LV}$ ,  $\gamma_{LS}$  and  $\gamma_{GS}$  are equilibrium liquid-gas, liquid-solid and gas-solid (in the approximation of undeformable solid substrate) surface tensions respectively. The Young-Dupré equation then was probed by evaluating independently surface tensions  $\gamma_{LV}$ ,  $\gamma_{LS}$  and  $\gamma_{GS}$  from microscopic stress tensor disregarding solid-to-solid interactions<sup>29</sup> and by directly measuring  $\theta_0$  from equilibrium free-surface profiles.

Surface tensions were evaluated using different geometrical set-ups with the duration of the averaging varied from  $1000 \tau_0$  to  $5000 \tau_0$  depending on the signal-to-noise ratio. Liquid-solid surface tension of the liquid  $\gamma_{LS}$  was calculated using a plane film of thickness ranging from  $16 \sigma_{ff}$  to  $25 \sigma_{ff}$  set on the substrate with lateral dimensions  $20 \times 20 \sigma_{ff}$ . We used periodic boundary conditions in the tangential to the substrate directions and averaging over five statistically independent observations with randomly generated surface roughness. Liquid-gas surface tension  $\gamma_{LV}$  was obtained in levitating, radius  $\approx 30 \sigma_{ff}$ , spherical drops.<sup>41</sup> At the same time, gas-solid surface tension of the gas  $\gamma_{GS}$  was evaluated directly in the static simulations of droplets on the bandwidth of  $\Delta z = 10 \sigma_{ff}$  of the substrate away from the contact line using five independent measurements. One needs to note that the gas phase was practically absent, and the surface tension  $\gamma_{GS}$  was zero in all cases but one with monatomic particles, run (e), Table 1. The difference between two static contact angles (measured geometrically and calculated *via* the Young-Dupré equation) was found not to exceed the accuracy of the contact angle evaluations, Table 1.

## Acknowledgement

This paper is dedicated to the memory of my friend and colleague, Alexei Likhtman, who recently passed away. The authors are grateful to T. Blake and J. De Coninck for useful discussions.

## References

1. de Gennes, P.G. Wetting: Statics and Dynamics. *Rev. Mod. Phys.* **1985**, 57, 827–863
2. Squires, T.M.; Quake, S.R. Microfluidics: Fluid Physics at the Nanoliter Scale *Ann. Rev. Fluid Mech.* **2005**, 77, 977–1026

3. Stone, H.A.; Stroock, A.D.; Ajdari, A. Engineering Flows in Small Devices: Microfluidics Toward a Lab-on-a-Chip *Rev. Mod. Phys.* **2004**, 36, 381–411
4. Blake, T.D.; Ruschak, K.J. A Maximum Speed of Wetting. *Nature* **1979**, 282, 489–491
5. Voinov, O.V. Hydrodynamics of Wetting. *Fluid Dyn.* 11, 714–721 **1976**,
6. Dussan, E.B. On the Spreading of Liquids on Solid Surfaces: Static and Dynamic Contact Lines *Ann. Rev. Fluid Mech.* **1979**, 11, 371–400
7. Blake, T.D.; Haynes, J.M. Kinetics of Liquid/Liquid Displacement. *J. Colloid Interface Sci.* **1969**, 30, 421–423
8. Cox, R.G. The Dynamics of the Spreading of Liquids on a Solid Surface. Part 1. Viscous Flow. *J. Fluid Mech.* **1986**, 168, 169–194
9. Koplik, J.; Banavar, J.R.; Willemsen, J.F. Molecular Dynamics of Poiseuille Flow and Moving Contact Lines. *Phys. Rev. Lett.* **1988**, 60, 1282–1285
10. Thompson, P.A.; Robbins, M.O. Simulations of Contact-Line Motion: Slip and the Dynamic Contact Angle. *Phys. Rev. Lett.* **1989**, 63, 766–769
11. Ondarcuhu, T.; Veyssie, M. Relaxation Modes of the Contact Line of a Liquid Spreading on a Surface. *Nature* **1991**, 352, 418–420
12. Marsh, J.A.; Garoff, S.; Dussan, E.B.V. Dynamic Contact Angles and Hydrodynamics Near a Moving Contact Line. *Phys. Rev. Lett.* **1993**, 70, 2778–2781
13. Chen, Q.; Rame, E.; Garoff, S. The Velocity Field Near Moving Contact Lines *J. Fluid Mech.* **1997**, 337, 49–66
14. Schneemilch, M.; Hayes, R.A.; Petrov, J.G.; Ralston, J. Dynamic Wetting and Dewetting of a Low-Energy Surface by Pure Liquids. *Langmuir* **1998**, 14, 7047–7051
15. Blake, T.D. The Physics of the Moving Wetting Lines. *AIChE J* **2006**, 299, 1–13

16. Shikhmurzaev, Y.D. *Capillary Flows with Forming Interfaces*. (Taylor & Francis, 2007).
17. Ralston, J.; Popescu, M.; Sedev, R. Dynamics of Wetting from an Experimental Point of View *Ann. Rev. Mater. Res.* **2008**, 38, 23–43
18. Bonn, D.; Eggers, J.; Indekeu, J.; Meunier, J.; Rolley, E. Wetting and Spreading *Rev. Mod. Phys.* **2009**, 81, 739–805
19. De Coninck, J.; Blake, T.D. Wetting and Molecular Dynamics Simulations of Simple Liquids. *Annu. Rev. Mater. Res.* **2008**, 38, 1–22
20. Bertrand, E.; Blake, T.D.; De Coninck, J. Influence of Solid-Liquid Interactions on Dynamic Wetting: a Molecular Dynamics Study. *J. Phys.: Condens. Matter* **2009**, 21, 464124
21. Duvivier, D.; Blake, T.D.; De Coninck, J. Toward a Predictive Theory of Wetting Dynamics. *Langmuir* **2013**, 29, 10132–10140
22. Snoeijer, J.H.; Andreotti, B. Moving Contact Lines: Scales, Regimes, and Dynamical Transitions. *Annu. Rev. Fluid Mech.* **2013**, 45, 269–292
23. Jacqmin, D. Contact-Line Dynamics of a Diffuse Fluid Interface. *J. Fluid Mech.* **2000**, 402, 57–88
24. Ding, H.; Spelt, P.D.M. Wetting Condition in Diffuse Interface Simulations of Contact Line Motion *Phys. Rev. E* **2007**, 75, 046708
25. Briant, A.J.; Wagner, A.J.; Yeomans, J.M. Lattice Boltzmann Simulations of Contact Line Motion. I. Liquid-gas systems. *Phys. Rev. E* **2004**, 69, 031602
26. Nakamura, Y.; Carlson, A.; Amberg, G.; Shiomi, J. Dynamic Wetting at the Nanoscale. *Phys. Rev. E* **2013**, 88, 033010

27. Kirkinis, E.; Davis, S.H. Hydrodynamic Theory of Liquid Slippage on a Solid Substrate Near a Moving Contact Line. *Phys. Rev. Lett.* **2013**, 110, 234503
28. Chen, L.; Yu, J.; Wang, H. Convex Nanobending at a Moving Contact Line: The Missing Mesoscopic Link in Dynamic Wetting. *ACS Nano* **2014**, 8, 11493-11498
29. Lukyanov, A.V.; Likhtman, A.E. Relaxation of Surface Tension in the Liquid-Solid Interfaces of Lennard-Jones Liquids. *Langmuir* **2013**, 29, 13996–14000
30. Aarts, D.G.A.L.; Schmidt, M.; Lekkerkerker, H.N.W. Direct Visual Observation of Thermal Capillary Waves *Science* **2004**, 304, 847–850
31. Thompson, P.A.; Troian, S.M. A General Boundary Condition for Liquid Flow at Solid Surfaces. *Nature* 389, 360–362 **1997**,
32. Priezjev, N.V. Relationship Between Induced Fluid Structure and Boundary Slip in Nanoscale Polymer Films. *Phys. Rev. E* **2010**, 82, 051603
33. Barrat, J.-L.; Bocquet, L. Influence of Wetting Properties on Hydrodynamic Boundary Conditions at a Fluid/Solid Interface. *Faraday Discuss.* **1999**, 112, 119-127
34. Bocquet, L.; Barrat, J.-L. Flow Boundary Conditions from Nano- to Micro-Scales. *Soft Matter* **2007**, 3, 685-693
35. Priezjev, N.V.; Troian, S.M. Molecular Origin and Dynamic Behavior of Slip in Sheared Polymer Films. *Phys. Rev. Lett.* **2004**, 92, 018302
36. Meier, K.; Laesecke, A.; Kabelac, S. Transport Coefficients of the Lennard-Jones Model Fluid. II Self-Diffusion. *J. Chem. Phys.* **2004**, 121, 9526–9535
37. Likhtman, A.E.; Sukumaran, S.K.; Ramirez, J. Linear Viscoelasticity from Molecular Dynamics Simulation of Entangled polymers. *Macromolecules* **2007**, 40, 6748-6757

- 38. Glasstone, S.; Laidler, K.J.; Eyring, H. *The Theory of Rate Processes*. (McGraw-Hill Book Co., Inc., New York City, 1941).
- 39. Kremer, K.; Grest, G.S. Dynamics of Entangled Linear Polymer Melts: A Molecular-Dynamics Simulation. *J. Chem. Phys.* **1990**, 92, 5057–5086
- 40. Weijs, J.H.; Andreotti, B.; Snoeijer, J.H. Elasto-Capillarity at the Nanoscale: on the Coupling Between Elasticity and Surface Energy in Soft Solids. *Soft Matter* **2013**, 9, 8494–8503
- 41. Lukyanov, A.V.; Likhtman, A.E. Relaxation of Surface Tension in the Free-Surface Boundary Layer of Simple Lennard-Jones Liquids. *J. Chem. Phys.* **2013**, 138, 034712

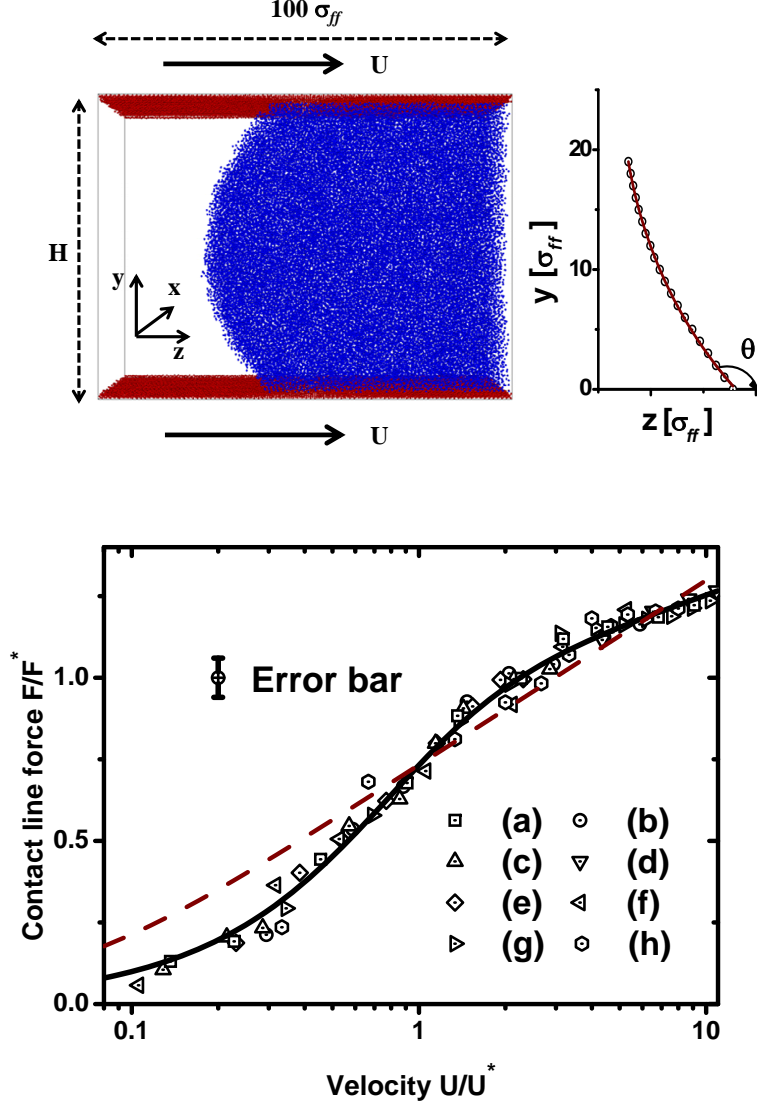


Figure 1: Snapshot of the moving cylindrical droplet (periodic in the  $x$ -direction) simulation set-up, developed free surface profile with dynamic contact angle  $\theta = 134^\circ$  (at the parameters of run (a), Table 1, at  $H = 60 \sigma_{ff}$  and  $U = 0.07 u_0$ ,  $u_0 = \sqrt{\epsilon_{ff}/m_f}$ ) and a cumulative set of data, Table 1, represented as normalized contact line force  $F/F^*$  as a function of normalized substrate velocity  $U/U^*$ . The error bar shows the maximum deviation. The solid line is the fit  $F_c/F^* = \frac{U/U^*}{(1+(U/U^*)^2)^{0.45}}$ . The dashed line is the best fit  $F_c/F^* = \tilde{\chi} \ln \left( v/\tilde{V} + \sqrt{1 + (v/\tilde{V})^2} \right)$ ,  $v = U/U^*$ ,  $\tilde{\chi} = 0.25$ ,  $\tilde{V} = 0.1$ . The total number of liquid particles in the simulations was varied between 60,000 to 90,000. The solid wall was moving along the  $z$ -direction in the set-up aligned in the  $[1,0,0]$  crystallographic direction of the face-centred cubic lattice comprising the solid substrate. The free surface profiles were obtained using time averaging over 5,000  $\tau_0$  following an equilibration period of 10,000  $\tau_0$  ( $\tau_0 = \sigma_{ff} \sqrt{\frac{m_f}{\epsilon_{ff}}}$ ) to reach a steady state.



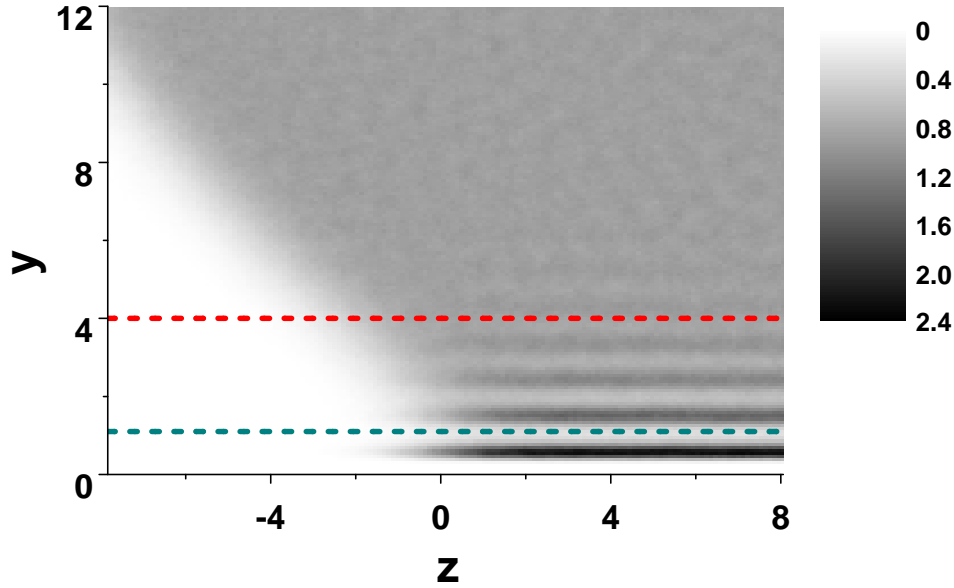


Figure 2: Distribution of the density at the contact line region of a moving droplet, Fig. 1, averaged over the droplet depth  $\Delta x \approx 18 \sigma_{ff}$  and a time period  $\Delta t = 5,000 \tau_0$  at parameters of run (a) in Table 1, at  $H = 60 \sigma_{ff}$  and  $U = 0.1 u_0$ ,  $u_0 = \sqrt{\epsilon_{ff}/m_f}$ . Distance  $z$  is measured along the substrate from the equimolar point of the surface density distribution  $\rho_s(z)$ , Fig. 3(d), and distance  $y$  is measured in the perpendicular to the substrate direction from the equimolar point of the substrate particle distribution. The dark region corresponds to the liquid phase. The dashed lines designate cut-off of the liquid-solid interface at  $y = 4 \sigma_{ff}$  (red line) and the observation region of the friction force, surface density and surface velocity distributions at  $y = 1.1 \sigma_{ff}$  (blue line).

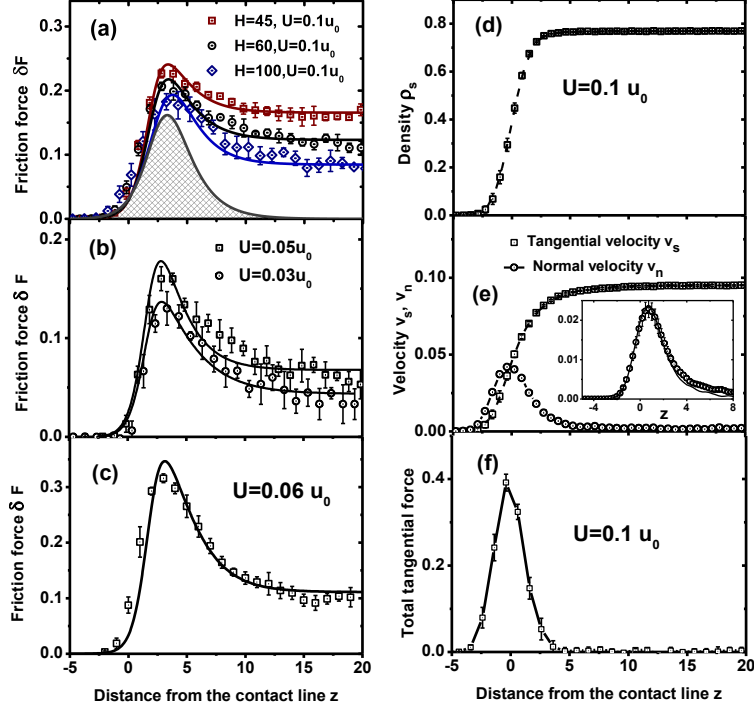


Figure 3: Distribution of the tangential friction force  $\delta F$ , surface density  $\rho_S$ , tangential and normal components of surface velocity,  $v_s$  and  $v_n$ , and the total force acting on the boundary layer  $\Delta y = 1.1$  adjacent to the substrate  $\delta F + f_{LL}$  as functions of the distance  $z$  from the equimolar point at the parameters from Table 1. All distributions were obtained after initial equilibration for  $10,000 \tau_0$  and averaging over five independent simulations each for  $10,000 \tau_0$  ( $\tau_0 = \sigma_{ff} \sqrt{\frac{m_f}{\epsilon_{ff}}}$ ). (a)  $\delta F(z)$ , run (a) at different droplet widths  $H = 100, 60$  and  $45 \sigma_{ff}$ , and  $U = 0.1 u_0$ ,  $u_0 = \sqrt{\epsilon_{ff}/m_f}$ . Symbols are direct MD simulations and the solid lines are the distributions  $\delta F_m(z)$  calculated by means of equation (2). The shaded area is the distribution  $\delta F_m$  in macroscopic limit  $v_\infty = U$  at  $U = 0.1 u_0$ ,  $H = 100 \sigma_{ff}$  and  $B^* = -0.94$ . (b)  $\delta F(z)$ , run (a) at  $H = 60 \sigma_{ff}$ , but at lower velocities  $U = 0.05 u_0$  and  $U = 0.03 u_0$ . Symbols are direct MD simulations and the solid lines are the distributions  $\delta F_m(z)$  calculated by means of equation (2). (c)  $\delta F(z)$ , run (d) at  $H = 60 \sigma_{ff}$  and  $U = 0.06 u_0$ . Symbols are direct MD simulations and the solid line is the distribution  $\delta F_m(z)$  calculated by means of equation (2). (d)  $\rho_S(z)$ , run (a) at  $H = 60 \sigma_{ff}$  and  $U = 0.1 u_0$ . Symbols are for direct MD simulations and the dashed line is the fit  $\rho_\infty \psi(z)$ . (e)  $v_s(z)$  and  $v_n(z)$ , run (a) at  $H = 60 \sigma_{ff}$  and  $U = 0.1 u_0$ . Symbols are direct MD simulations and the dashed line through the  $v_s$  profile is  $v_\infty f_v(z)$ . Inset illustrates conservation of mass in the the boundary layer  $\Delta y = 1.1$ ,  $\rho_s v_n = \rho_s \Delta y \frac{\partial v_s}{\partial z}$ , that is normal flux  $\rho_s v_n$  shown by symbols and  $\rho_s \Delta y \frac{\partial v_s}{\partial z}$  shown by the solid line. (f)  $\delta F(z) + f_{LL}(z)$ , run (a) at  $H = 60 \sigma_{ff}$  and  $U = 0.1 u_0$ .

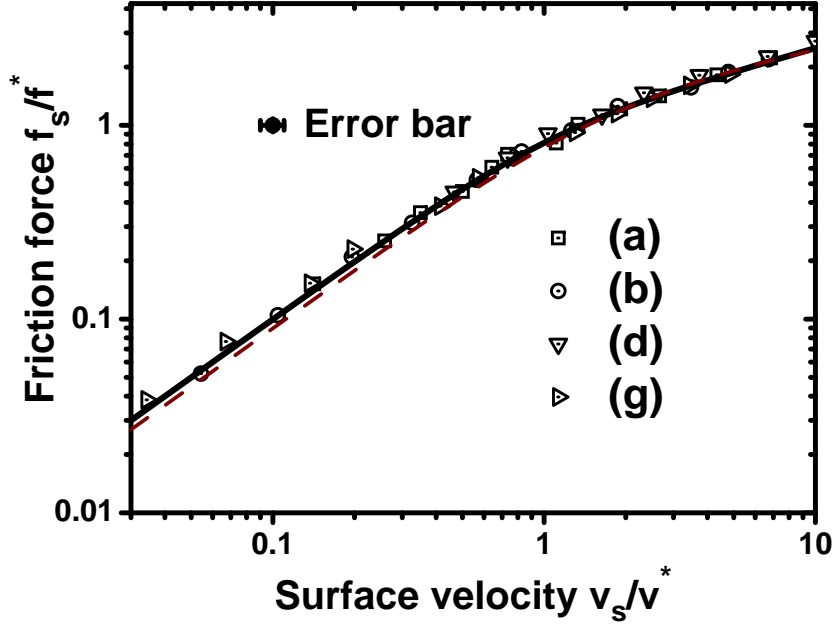


Figure 4: Surface friction force per unit area  $f_s$  as a function of surface velocity  $v_s$ . The data (symbols) were obtained in rectilinear Hagen-Poiseuille flow driven by external force applied to each liquid particle for the parameters listed in Table 1 after initial equilibration for  $5,000 \tau_0$  and averaging over  $5,000 \tau_0$  ( $\tau_0 = \sigma_{ff} \sqrt{\frac{m_f}{\epsilon_{ff}}}$ ) in two different intervals of the width  $\Delta z = 10 \sigma_{ff}$ . The flow direction to the solid wall lattice was the same as in the droplets simulations, Fig. 1. The solid line is the function  $f_s = f^* \frac{v_s/v^*}{(1+(v_s/v^*)^2)^{0.3}}$ . The dashed line is the function  $f/f^* = \tilde{\chi} \ln(v/\tilde{V} + \sqrt{1 + (v/\tilde{V})^2})$ ,  $v = v_s/v^*$ ,  $\tilde{\chi} = 0.8$ ,  $\tilde{V} = 0.9$ .

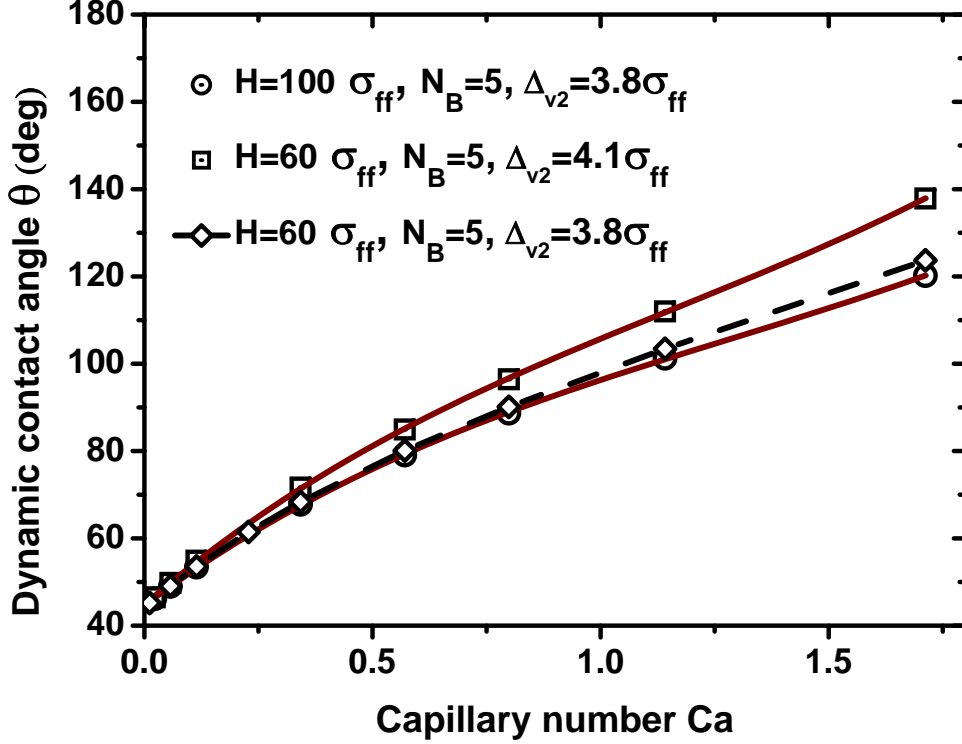


Figure 5: Dynamic contact angle  $\theta$  as a function of capillary number  $Ca = \mu U / \gamma_{LV}$  in the macroscopic limit  $H \gg 1$ ,  $v_\infty = U$  calculated from the modified Young-Dupré equation  $\gamma_{LV} \cos \theta = -\gamma_{LS} + \gamma_{GS} - F$  by means of relationship (3) at  $\lambda = 0.3$ . There were used parameters of run (a) from Table 2 giving the best fit to the distribution of the force in Fig. 3(a) at  $H = 100 \sigma_{ff}$  and  $H = 60 \sigma_{ff}$ , and  $U = 0.1 u_0$ . Symbols are the calculated values of the contact angle  $\theta$  and the solid lines are the fit  $\theta = \theta_0 + A Ca + B Ca^2 + C Ca^3$  at  $A \approx 78, B \approx -35, C \approx 9$  for  $H = 100 \sigma_{ff}$  and  $A \approx 91, B \approx -42, C \approx 11$  for  $H = 60 \sigma_{ff}$ . The dashed line is the guide for eyes in the case  $H = 60 \sigma_{ff}$ , but with  $\Delta_{v2} = 3.8 \sigma_{ff}$ .